







**Evidence of unconventional pairing in the quasi-two-dimensional  $\text{CuIr}_{2-x}\text{Ru}_x\text{Te}_4$  superconductor**

T. Shang <sup>1,\*</sup>,† Y. Chen,<sup>2,\*</sup> W. Xie,<sup>3,4</sup> D. J. Gawryluk <sup>5</sup> R. Gupta,<sup>6</sup> R. Khasanov <sup>6</sup> X. Y. Zhu,<sup>1</sup> H. Zhang,<sup>1</sup> Z. X. Zhen,<sup>1</sup> B. C. Yu,<sup>1</sup> Z. Zhou,<sup>7</sup> Y. Xu <sup>1</sup> Q. F. Zhan <sup>1</sup> E. Pomjakushina,<sup>5</sup> H. Q. Yuan,<sup>2</sup> and T. Shiroka <sup>6,8</sup>

<sup>1</sup>Key Laboratory of Polar Materials and Devices (MOE), School of Physics and Electronic Science, East China Normal University, Shanghai 200241, China

<sup>2</sup>Center for Correlated Matter and Department of Physics, Zhejiang University, Hangzhou 310058, China

<sup>3</sup>Institute of High Energy Physics, Chinese Academy of Sciences, Beijing 100049, China

<sup>4</sup>Spallation Neutron Source Science Center, Dongguan 523803, China

<sup>5</sup>Laboratory for Multiscale Materials Experiments, Paul Scherrer Institut, CH-5232 Villigen PSI, Switzerland

<sup>6</sup>Laboratory for Muon-Spin Spectroscopy, Paul Scherrer Institut, CH-5232 Villigen PSI, Switzerland

<sup>7</sup>Key Laboratory of Nanophotonic Materials and Devices & Key Laboratory of Nanodevices and Applications, Suzhou Institute of Nano-Tech and Nano-Bionics (SINANO), CAS, Suzhou 215123, China

<sup>8</sup>Laboratorium für Festkörperphysik, ETH Zürich, CH-8093 Zürich, Switzerland



(Received 31 July 2022; accepted 29 September 2022; published 13 October 2022)

The  $\text{CuIr}_{2-x}\text{Ru}_x\text{Te}_4$  superconductors (with a  $T_c$  around 2.8 K) can host charge-density waves, whose onset and interplay with superconductivity are not well known at a microscopic level. Here, we report a comprehensive study of the  $x = 0$  and 0.05 cases, whose superconductivity was characterized via electrical-resistivity, magnetization, and heat-capacity measurements, while their microscopic superconducting properties were studied via muon-spin rotation and relaxation ( $\mu\text{SR}$ ). In  $\text{CuIr}_{2-x}\text{Ru}_x\text{Te}_4$ , both the temperature-dependent electronic specific heat and the superfluid density (determined via transverse-field  $\mu\text{SR}$ ) are best described by a two-gap ( $s + d$ )-wave model, comprising a nodeless gap and a gap with nodes. The multigap superconductivity is also supported by the temperature dependence of the upper critical field  $H_{c2}(T)$ . However, under applied pressure, a charge-density-wave order starts to develop and, as a consequence, the superconductivity of  $\text{CuIr}_2\text{Te}_4$  achieves a more conventional  $s$ -wave character. Our series of experiments provides ample evidence that the  $\text{CuIr}_{2-x}\text{Ru}_x\text{Te}_4$  family belongs to the rare cases where an unconventional superconducting pairing is found near a charge-density-wave quantum critical point.

DOI: [10.1103/PhysRevB.106.144505](https://doi.org/10.1103/PhysRevB.106.144505)

## I. INTRODUCTION

The interplay between different electronic ground states is one of the fundamental topics in current condensed-matter physics. Notably, the materials exhibiting high-temperature- or unconventional superconductivity (SC), such as, e.g., heavy fermions, cuprates, or iron-based superconductors [1–4], are particularly relevant in this respect since, in most of them, the different types of order are closely related or even competing. Materials which sustain a charge-density-wave (CDW) order are renowned as suitable systems for investigating the coexistence and interplay between these different ground states [5–9]. The  $AT_2X_4$  chalcogenides (with  $A, T =$  transition metals, and  $X = \text{O, S, Se, Te}$ ) belong to this class and exhibit varied crystal structures with intriguing electronic properties. In particular, the  $\text{CuT}_2\text{X}_4$  family has attracted special attention due to its multifaceted ground states, including also SC and CDW. For instance,  $\text{CuIr}_2\text{S}_4$  undergoes a metal-to-insulator transition at 230 K [10–12], which is suppressed via Cu-Zn substitution to give rise to a dome-like SC phase (with maximum  $T_c = 3.4$  K) [13]. Similarly, in the  $\text{CuIr}_2\text{Se}_4$  case,

superconductivity with  $T_c = 1.76$  K can be induced via Ir-Pt substitution [14]. Furthermore,  $\text{CuV}_2\text{S}_4$  is known to exhibit three different CDW transitions (between 55 and 90 K) before it enters the SC phase at  $T_c = 4.4$  K [15]. Although hundreds of  $AT_2X_4$ -type materials have been discovered and examined, superconductivity has only been found in Cu-based sulpho- or seleno-spinels. An exception to this are telluride spinels (yet another chalcogen), which adopt lower-dimensional crystal structures compared with the S- or Se-based spinels, with  $\text{CuIr}_2\text{Te}_4$  recently shown to display SC [16]. Since, unlike the preceding group-16 elements, Te is a metalloid, we expect the  $\text{CuIr}_2\text{Te}_4$  properties to differ from those of S or Se compounds.

$\text{CuIr}_2\text{Te}_4$  crystallizes in a disordered trigonal structure with space group  $P\bar{3}m1$  (No. 164), where the Cu atoms and vacancies are randomly distributed in the Cu layers.  $\text{CuIr}_2\text{Te}_4$  exhibits a quasi-two-dimensional crystal structure, where  $\text{IrTe}_2$  layers are intercalated by Cu planes (see inset in Fig. 1). Such “sandwich-like” structure is also encountered in  $\text{Cu}_x\text{Bi}_2\text{Se}_3$  [17], a prime example of topological superconductor [18].  $\text{CuIr}_2\text{Te}_4$  undergoes a first-order CDW transition around 250 K, where both the electrical resistivity and magnetization exhibit clear anomalies, with a significant temperature hysteresis [16,19]. More interestingly, by further decreasing the temperature below  $T_c = 2.5$  K,  $\text{CuIr}_2\text{Te}_4$

\*These authors contributed equally to this work.

†tshang@phy.ecnu.edu.cn

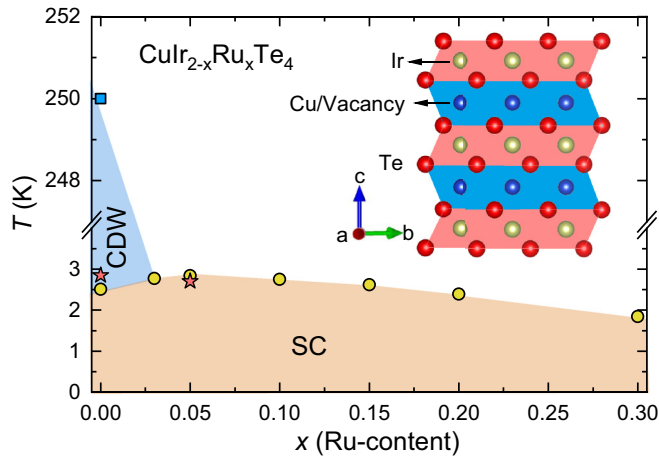


FIG. 1. Phase diagram of  $\text{CuIr}_{2-x}\text{Ru}_x\text{Te}_4$ . Stars refer to the current work, while the other symbols represent data taken from Ref. [20]. The CDW transition temperature  $T_{\text{CDW}}$  was determined from the temperature-dependent electrical resistivity, while the superconducting transition temperatures  $T_c$  were derived from magnetic-susceptibility measurements. The inset shows the crystal structure of  $\text{CuIr}_2\text{Te}_4$  (i.e., without depicting the Cu vacancies) viewed along the [100] direction, clearly demonstrating its quasi-two-dimensional character. Blue, yellow, and red spheres represent Cu, Ir, and Te atoms, respectively.

becomes a superconductor [16]. Upon substituting Ir with Ru, in  $\text{CuIr}_{2-x}\text{Ru}_x\text{Te}_4$ , the CDW order is quickly suppressed at  $x = 0.03$ , while the superconducting transition temperature increases up to 2.8 K (for  $x = 0.05$ , see Fig. 1) [20]. Similar features have been found also in Al-, Ti-, and Zr-substituted  $\text{CuIr}_2\text{Te}_4$  [21–23]. Although at low doping, Cr-substituted  $\text{CuIr}_2\text{Te}_4$  samples show similar behavior to the above families, once the Cr content is above 0.25 (i.e.,  $x > 0.25$ ), a ferromagnetic order occurs [24]. Such dome-like superconducting phase resembles that of unconventional superconductors [1–4] and transition-metal dichalcogenides [5,6]. As in them, also in  $\text{CuIr}_2\text{Te}_4$  the dome may signal the presence of a CDW quantum critical point (QCP), with the increase in  $T_c$  reflecting the enhanced quantum fluctuations near such QCP. Upon increasing the Ru content above  $x = 0.3$ , the SC is destroyed. According to electronic band-structure calculations, the density of states near the Fermi level consists mostly of Te- $p$  and Ir- $d$  orbitals [16], both characterized by a large spin-orbit coupling, potentially leading to unconventional superconducting properties. Here, the competition between CDW and SC is possibly tuned by modifications of the density of states and Fermi surface via chemical doping.

Since in  $\text{CuIr}_2\text{Te}_4$ , both CDW and SC can be easily tuned via chemical substitution, this represents an ideal system for investigating the interplay between the two. Although certain properties of the  $\text{CuIr}_{2-x}\text{Ru}_x\text{Te}_4$  family have been examined and electronic band-structure calculations are available, at a microscopic level its superconducting properties, in particular the superconducting order parameter, have not been explored and await further investigation.

In this work, after synthesizing  $\text{CuIr}_{2-x}\text{Ru}_x\text{Te}_4$  ( $x = 0$  and 0.05) samples, we systematically studied their superconducting properties by means of electrical-resistivity,

magnetization, and heat-capacity measurements, complemented by the muon-spin relaxation and rotation ( $\mu\text{SR}$ ) method. Certain measurements were also performed under external pressure (up to 2.5 GPa). Both the superfluid density and the electronic specific heat of  $\text{CuIr}_{2-x}\text{Ru}_x\text{Te}_4$  are best described by a two-gap model, consisting of a nodeless gap and a gap with nodes. The observation of a nodal gap is our key finding, which suggests the  $\text{CuIr}_{2-x}\text{Ru}_x\text{Te}_4$  family to be a remarkable system, where competing orders can lead to unconventional SC behavior.

## II. EXPERIMENTAL DETAILS

Polycrystalline  $\text{CuIr}_{2-x}\text{Ru}_x\text{Te}_4$  samples, with  $x = 0$  and 0.05, were prepared by the solid-state reaction method (the details can be found in Ref. [20]). The crystal structure and phase purity were checked by powder x-ray diffraction, confirming the trigonal structure of  $\text{CuIr}_{2-x}\text{Ru}_x\text{Te}_4$  ( $P\bar{3}m1$ , No. 164). The superconductivity was characterized by electrical-resistivity, heat-capacity, and magnetization measurements, performed on a Quantum Design physical property measurement system (PPMS) and a magnetic property measurement system (MPMS), respectively. For the electrical-resistivity and ac-susceptibility measurements under pressure we employed a BeCu piston-cylinder cell, with Daphne oil 7373 used as the pressure transmitting medium.

The bulk  $\mu\text{SR}$  measurements were carried out at the multipurpose surface-muon spectrometer (Dolly) of the Swiss muon source at Paul Scherrer Institut, Villigen, Switzerland. In this study, we performed mostly transverse-field (TF)  $\mu\text{SR}$  measurements, which allowed us to determine the temperature evolution of the magnetic penetration depth and thus of the superfluid density. All the  $\mu\text{SR}$  spectra were collected upon heating and were analyzed by means of the MUSRFIT software package [25].

## III. RESULTS AND DISCUSSION

### A. Lower and upper critical fields

The bulk superconductivity of  $\text{CuIr}_{2-x}\text{Ru}_x\text{Te}_4$  was first characterized by magnetic-susceptibility measurements, using both field-cooled (FC) and zero-field-cooled (ZFC) protocols in an applied field of 1 mT. As shown in Fig. 2(a), a clear diamagnetic signal appears below the superconducting transition at  $T_c = 2.85$  and 2.7 K for  $\text{CuIr}_2\text{Te}_4$  and  $\text{CuIr}_{1.95}\text{Ru}_{0.05}\text{Te}_4$ , respectively. The rather sharp transitions (with a  $\Delta T \approx 0.1$  K, three times smaller than in a previous work [16]) indicate a good sample quality. After accounting for the demagnetizing factor, the superconducting shielding fraction of both samples is  $\approx 100\%$ , indicative of bulk SC, as further confirmed by heat-capacity and  $\mu\text{SR}$  measurements (see below). To determine the lower critical field  $H_{c1}$ , essential for performing  $\mu\text{SR}$  measurements on type-II superconductors, the field-dependent magnetization  $M(H)$  was collected at various temperatures. The  $M(H)$  curves are shown in Figs. 2(c) and 2(d) for  $\text{CuIr}_2\text{Te}_4$  and  $\text{CuIr}_{1.95}\text{Ru}_{0.05}\text{Te}_4$ , respectively. The estimated  $H_{c1}$  values (accounting for the demagnetization factor) as a function of temperature are summarized in Fig. 2(b). They result in  $\mu_0 H_{c1}(0) = 13.5(3)$  and 11.9(3) mT for the pure and the Ru-substituted sample, respectively.

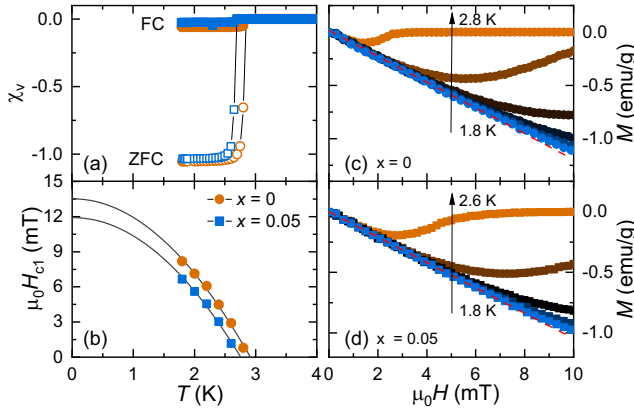


FIG. 2. (a) Temperature-dependent magnetic susceptibility  $\chi_V(T)$  of  $\text{CuIr}_{2-x}\text{Ru}_x\text{Te}_4$ , with  $x = 0$  and  $0.05$ . The ZFC and FC magnetic susceptibilities were measured in a field of  $\mu_0 H = 1$  mT. (b) Lower critical fields  $H_{c1}$  vs temperature. Solid lines are fits to  $\mu_0 H_{c1}(T) = \mu_0 H_{c1}(0)[1 - (T/T_c)^2]$ . Field-dependent magnetization curves collected at various temperatures after cooling the (c)  $\text{CuIr}_2\text{Te}_4$  and (d)  $\text{CuIr}_{1.95}\text{Ru}_{0.05}\text{Te}_4$  samples in zero field. For each temperature,  $H_{c1}$  is determined as the value where  $M(H)$  starts deviating from linearity [dashed lines in panels (c) and (d)].

To investigate the upper critical field  $H_{c2}$  of  $\text{CuIr}_{2-x}\text{Ru}_x\text{Te}_4$ , measurements of the temperature-dependent electrical resistivity  $\rho(T, H)$  and specific heat  $C(T, H)/T$  at various applied magnetic fields, as well as the field-dependent magnetization  $M(H, T)$  at various temperatures were performed. These results are summarized in Figs. 3(a)–3(c) and 3(d)–3(f) for  $\text{CuIr}_2\text{Te}_4$  and  $\text{CuIr}_{1.95}\text{Ru}_{0.05}\text{Te}_4$ , respectively. The distinct specific-heat jump at  $T_c$  again confirms the bulk nature of SC in  $\text{CuIr}_{2-x}\text{Ru}_x\text{Te}_4$ . Upon increasing the magnetic field, the superconducting transition in  $\rho(T)$  and  $C(T)/T$  shifts to lower temperatures. In the  $M(H)$  data, the diamagnetic signal vanishes once the applied magnetic field exceeds the upper critical field  $H_{c2}$ , as indicated by the arrows in Figs. 3(b) and 3(f). We found that the onset of zero resistivity corresponds to the midpoint of the superconducting transition in the specific heat (indicated by dashed lines in Fig. 3).

The upper critical fields  $H_{c2}$  vs the reduced superconducting temperatures  $T_c/T_c(0)$  are summarized in Figs. 4(a) and 4(b) for  $\text{CuIr}_2\text{Te}_4$  and  $\text{CuIr}_{1.95}\text{Ru}_{0.05}\text{Te}_4$ , respectively. To determine the upper critical field at 0 K, the  $H_{c2}(T)$  data were first analyzed by means of a Werthamer-Helfand-Hohenberg (WHH) model [26]. As shown by the solid lines in Fig. 4, the WHH model can describe the experimental data reasonably well up to  $0.075$  T. At higher magnetic fields, though, this model fails to follow the data and underestimates  $H_{c2}$  values. By contrast,  $H_{c2}(T)$  seem to exhibit a linear temperature dependence. As indicated by the dash-dotted lines, a linear fit agrees remarkably well with the experimental data and provides  $\mu_0 H_{c2}(0) = 0.212(1)$ , and  $0.241(1)$  T for  $\text{CuIr}_2\text{Te}_4$  and  $\text{CuIr}_{1.95}\text{Ru}_{0.05}\text{Te}_4$ , respectively. Both  $H_{c2}(0)$  values are well below the weak-coupling Pauli-limit value (i.e.,  $1.86T_c \approx 5$  T), suggesting that the orbital pair-breaking effect is dominant in  $\text{CuIr}_{2-x}\text{Ru}_x\text{Te}_4$  superconductors. A linear  $H_{c2}(T)$  over a wide temperature

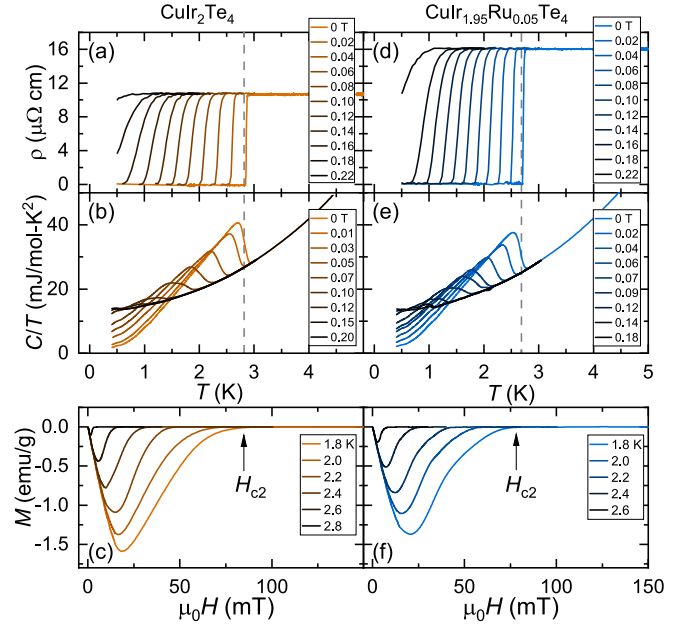


FIG. 3. (a) Temperature-dependent electrical resistivity  $\rho(T, H)$  and (b) specific heat  $C(T, H)/T$  for  $\text{CuIr}_2\text{Te}_4$  measured at various applied magnetic fields. (c) Field-dependent magnetization  $M(H, T)$  collected at various temperatures for  $\text{CuIr}_2\text{Te}_4$ . (d)–(f) The analogous results for  $\text{CuIr}_{1.95}\text{Ru}_{0.05}\text{Te}_4$ . For the  $\rho(T, H)$  measurements,  $T_c$  was defined as the onset of zero resistivity; for the  $C(T, H)/T$  measurements,  $T_c$  was defined as the midpoint of superconducting transition (marked by dashed lines). As indicated by arrows in panels (c) and (f),  $H_{c2}$  was chosen as the field where the diamagnetic response in  $M(H, T)$  vanishes.

range is uncommon. Recently, it has been observed, e.g., in infinite-layer nickelates  $\text{La}_{1-x}(\text{Sr}, \text{Ca})_x\text{NiO}_2$  and in noncentrosymmetric  $\text{ThCo}_{1-x}\text{Ni}_x\text{C}_2$  superconductors [27–29], the latter exhibiting line nodes in the superconducting gap [30]. A linear  $H_{c2}(T)$  deviates significantly from what is expected from a conventional BCS superconductor. As such, it strongly suggests an unconventional superconducting pairing in  $\text{CuIr}_{2-x}\text{Ru}_x\text{Te}_4$ .

In addition, in a single-band  $s$ -wave superconductor, the superfluid density is almost independent of temperature for  $T < T_c/3$ . As a result, in general,  $H_{c2}$  saturates at low temperatures, as clearly illustrated by the WHH model in Fig. 4. Conversely, in a multiband superconductor, the superfluid density in the nondominant band (typically the one with the smaller gap) increases with decreasing temperature (even below  $T_c/3$ ), thus leading to a continuously increasing  $H_{c2}$ . For example, typical multiband superconductors, such as  $\text{MgB}_2$  [31] and  $\text{Lu}_2\text{Fe}_3\text{Si}_5$  [32], exhibit a nonsaturating and almost linear  $H_{c2}(T)$ . Based on this, we reanalyzed  $H_{c2}(T)$  now using a two-band (TB) model [33]. As indicated by dotted lines in Fig. 4, the TB model, too, shows a good agreement with the experimental data and yields comparable  $H_{c2}(0)$  values. The multiband nature of  $\text{CuIr}_{2-x}\text{Ru}_x\text{Te}_4$  is further confirmed by the temperature-dependent superfluid density and electronic specific heat (see below), as well as by electronic band-structure calculations, where multiple bands are identified to cross the Fermi level [16].

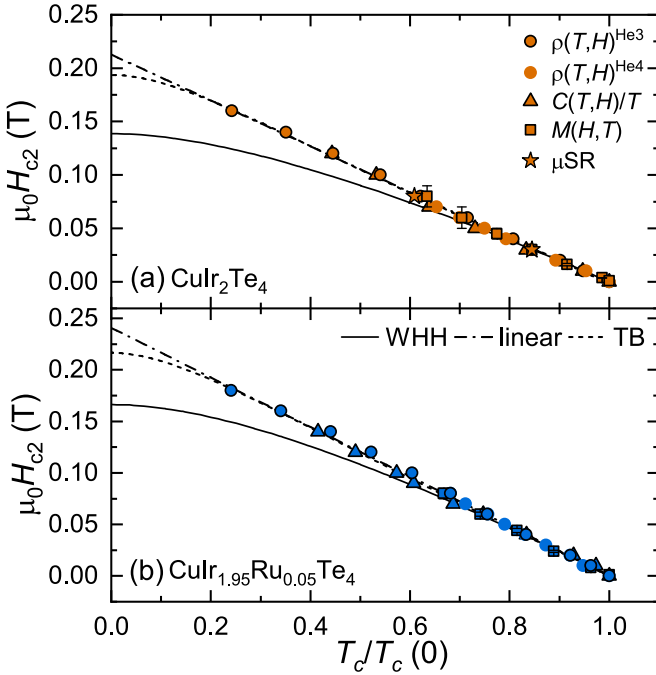


FIG. 4. Upper critical field  $H_{c2}$  vs the reduced superconducting transition temperature  $T_c/T_c(0)$  for (a)  $\text{CuIr}_2\text{Te}_4$  and (b)  $\text{CuIr}_{1.95}\text{Ru}_{0.05}\text{Te}_4$ . The  $T_c$  and  $H_{c2}$  values were determined from the measurements shown in Figs. 3 and 6, which are highly consistent. The temperature-dependent electrical resistivity was measured using both He-3 and He-4 cryostats. The solid and the dotted lines represent fits to the WHH and TB models, while the dash-dotted lines indicate a linear temperature dependence.

### B. Transverse-field and zero-field $\mu\text{SR}$

Since our pure- and Ru-doped  $\text{CuIr}_2\text{Te}_4$  samples share similar features and there is no clear CDW transition in the pure case (see below), most of our  $\mu\text{SR}$  measurements were performed on  $\text{CuIr}_2\text{Te}_4$ . To investigate its superconducting pairing, we carried out systematic temperature-dependent TF- $\mu\text{SR}$  measurements in applied magnetic fields of 30 and 80 mT. After cooling in an applied field, the TF- $\mu\text{SR}$  spectra were collected upon heating. Representative TF- $\mu\text{SR}$  spectra in the superconducting- and normal states of  $\text{CuIr}_2\text{Te}_4$  are shown in Fig. 5 for TF-30 mT. The normal-state spectra show essentially no damping, thus reflecting a uniform field distribution. Conversely, in the superconducting state (e.g., at 0.3 K), the significantly enhanced damping reflects the inhomogeneous field distribution due to the development of a flux-line lattice (FLL) [34–36]. The broadening of the field distribution in the SC phase is clearly visible in Fig. 5(b), where the fast-Fourier transform (FFT) spectra of the corresponding TF-30 mT  $\mu\text{SR}$  data are shown.

To properly describe the field distribution, the TF- $\mu\text{SR}$  spectra were modeled using [37]

$$A_{\text{TF}}(t) = \sum_{i=1}^n A_i \cos(\gamma_\mu B_i t + \phi) e^{-\sigma_i^2 t^2 / 2} + A_{\text{bg}} \cos(\gamma_\mu B_{\text{bg}} t + \phi). \quad (1)$$

Here  $A_i$  (97%),  $A_{\text{bg}}$  (3%) and  $B_i$ ,  $B_{\text{bg}}$  are the initial asymmetries and local fields sensed by implanted muons

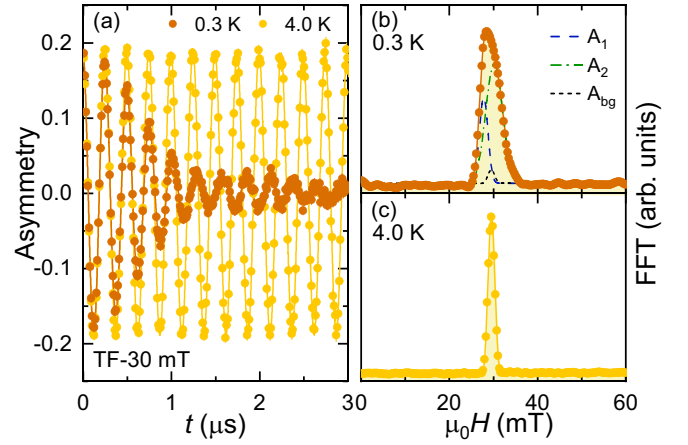


FIG. 5. (a) TF- $\mu\text{SR}$  spectra collected in an applied field of 30 mT in both the superconducting- and normal states of  $\text{CuIr}_2\text{Te}_4$ . The respective real part of the Fourier transforms of  $\mu\text{SR}$  spectra are shown in panels (b) and (c) for 0.3 and 4.0 K, respectively. Solid lines are fits to Eq. (1) using two oscillations. These are also shown separately as dashed- and dash-dotted lines in panel (b), together with a background contribution (dotted line). Analogous results, but with a single oscillation, were obtained for an applied field of 80-mT.

in the sample and sample holder,  $\gamma_\mu/2\pi = 135.53$  MHz/T is the muon gyromagnetic ratio,  $\phi$  is a shared initial phase, and  $\sigma_i$  is the Gaussian relaxation rate of the  $i$ th component. Here, we find that, while two oscillations (i.e.,  $n = 2$ ) are required to properly describe the TF-30 mT  $\mu\text{SR}$  spectra, a single oscillation is sufficient for the 80-mT spectra. In the 30-mT case, the dashed, dash-dotted, and dotted lines in Fig. 5(b) represent the two components at 0.3 K ( $A_1$  and  $A_2$ ) and the background signal ( $A_{\text{bg}}$ ), respectively. A similar behavior has been found in other superconductors, e.g.,  $\text{Mo}_3\text{P}$  or  $\text{ReBe}_{22}$  [38,39], where the  $\mu\text{SR}$  spectra collected at higher magnetic fields exhibit a more symmetric field distribution. For TF-30mT  $\mu\text{SR}$ , the effective Gaussian relaxation rate  $\sigma_{\text{eff}}$  can be calculated from  $\sigma_{\text{eff}}^2/\gamma_\mu^2 = \sum_{i=1}^2 A_i[\sigma_i^2/\gamma_\mu^2 - (B_i - \langle B \rangle)^2]/A_{\text{tot}}$  [37], where  $\langle B \rangle = (A_1 B_1 + A_2 B_2)/A_{\text{tot}}$  and  $A_{\text{tot}} = A_1 + A_2$ . Considering the constant nuclear relaxation rate  $\sigma_n$  in the narrow temperature range investigated here, confirmed also by zero-field (ZF-)  $\mu\text{SR}$  measurements (see below), the superconducting Gaussian relaxation rate can be extracted using  $\sigma_{\text{sc}} = (\sigma_{\text{eff}}^2 - \sigma_n^2)^{1/2}$ . Then, the superconducting gap value and its symmetry can be investigated by measuring the temperature-dependent  $\sigma_{\text{sc}}$ , which is directly related to the magnetic penetration depth and thus the superfluid density. Since the upper critical field of  $\text{CuIr}_2\text{Te}_4$  ( $\approx 0.2$  T) is not significantly large compared with the applied TF fields (30 and 80 mT), the effective penetration depth  $\lambda_{\text{eff}}$  had to be calculated from  $\sigma_{\text{sc}}$  by considering the overlap of the vortex cores. Consequently, in our case,  $\lambda_{\text{eff}}$  was calculated by means of  $\sigma_{\text{sc}} = 0.172 \frac{\gamma_\mu \Phi_0}{2\pi} (1-h)[1 + 1.21(1-\sqrt{h})^3] \lambda_{\text{eff}}^{-2}$  [40,41], where  $h = H_{\text{appl}}/H_{c2}$ , with  $H_{\text{appl}}$  being the applied magnetic field.

The inverse square of the magnetic penetration depth [proportional to the superfluid density, i.e.,  $\lambda_{\text{eff}}^{-2}(T) \propto \rho_{\text{sc}}(T)$ ] vs the reduced temperature  $T/T_c$  is shown in Figs. 6(a) and 6(b)

TABLE I. Summary of the superfluid-density and electronic specific-heat data analysis using different models for  $\text{CuIr}_2\text{Te}_4$ . In the gap function  $g_{\mathbf{k}}$ ,  $\theta$ , and  $\phi$  are the polar and azimuthal angles in  $k$  space. The SC gap values are in meV units, while the zero-temperature magnetic penetration depths  $\lambda_0$  are in nm. For the two-gap models, the numbers in the columns 5 and 6 refer to the first- and the second gap values. In the last column, the reduced least-square deviations  $\chi_r^2$  are reported for the TF  $\mu\text{SR}$  (30 mT) and  $C_e/T$  data, respectively. The weights listed in table refer to the first  $s$ -wave component.

Model	$g_{\mathbf{k}}$ function	Gap type	$\lambda_0$	$\Delta_0$ (TF $\mu\text{SR}$ )	$\Delta_0$ ( $C_e/T$ )	$\chi_r^2$ ( $\mu\text{SR} : C_e/T$ )
$s$ wave	1	Nodeless	183	0.36	0.43	6.4 : >30
$p$ wave	$\sin\theta$	Point-node	179	0.46	0.51	7.8 : 14.4
$d$ wave	$\cos 2\phi$	Line-node	170	0.54	0.57	23.1 : >30
$s + s$ (weighted)	1, 1	Nodeless	183	0.13/0.37(0.1)	0.12/0.44(0.15)	6.3 : 9.5
$s + d$ (weighted)	1, $\cos 2\phi$	Line-node	181	0.36/0.52(0.70)	0.45/0.54(0.57)	4.7 : 5.1

for TF-30 mT and TF-80 mT, respectively. In both cases, the superfluid density remains weakly temperature dependent down to the lowest temperature, i.e., below  $T_c/3$ . Such behavior indicates the presence of low-energy excitations and, hence, of nodes in the superconducting gap. To get further insight into the pairing symmetry, the superfluid density  $\rho_{\text{sc}}(T)$  was analyzed using different models, generally described by

$$\rho_{\text{sc}}(T) = 1 + 2 \left\langle \int_{\Delta_{\mathbf{k}}}^{\infty} \frac{E}{\sqrt{E^2 - \Delta_{\mathbf{k}}^2}} \frac{\partial f}{\partial E} dE \right\rangle_{\text{FS}}. \quad (2)$$

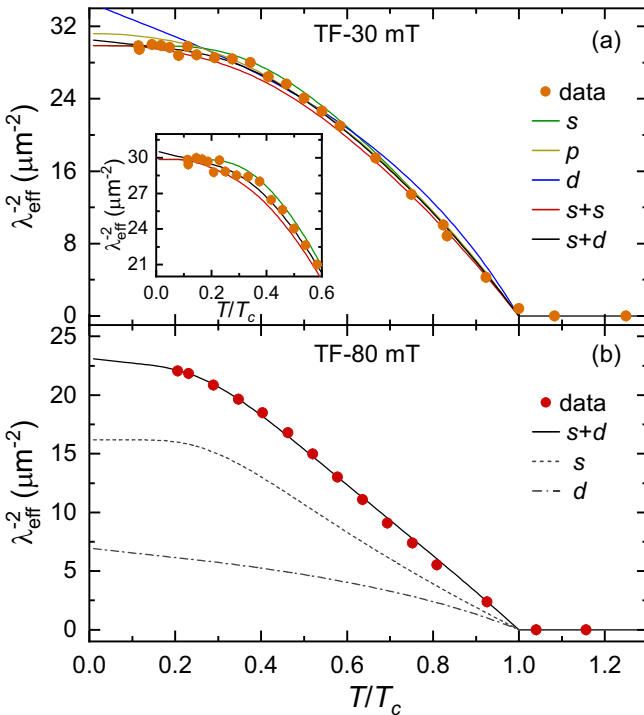


FIG. 6. Superfluid density vs temperature, as determined from TF- $\mu\text{SR}$  measurements in a magnetic field of (a) 30 mT and (b) 80 mT. The inset in panel (a) shows the enlarged plot below  $T/T_c = 0.6$ . The different lines represent fits to various models, including single-gap  $s$ ,  $p$ , and  $d$  wave, and two-gap ( $s + s$ ) and ( $s + d$ ) wave (see text for details). In the latter case, the  $s$  (dashed line) and  $d$  components (dash-dotted line) are also shown separately in panel (b) for the TF-80 mT case. All fit parameters are listed in Table I.

Here,  $f = (1 + e^{E/k_B T})^{-1}$  is the Fermi function and  $\langle \rangle_{\text{FS}}$  represents an average over the Fermi surface [42].  $\Delta_{\mathbf{k}}(T) = \Delta(T)g_{\mathbf{k}}$  is the product of  $\Delta(T)$ , the temperature-dependent gap, and  $g_{\mathbf{k}}$ , the angular dependence of the gap (see details in Table I). The temperature dependence of the gap is assumed to follow  $\Delta(T) = \Delta_0 \tanh\{1.82[1.018(T_c/T - 1)]^{0.51}\}$  [42,43], where  $\Delta_0$  is the gap value at 0 K.

Five different models, including single-gap  $s$ ,  $p$ , and  $d$  wave, and two-gap ( $s + s$ ) and ( $s + d$ ) wave, were used to analyze the  $\lambda_{\text{eff}}^{-2}(T)$  data. The derived fitting parameters are listed in Table I. As can be clearly seen in Fig. 6(a), the weak temperature dependence of the superfluid density at low- $T$  rules out a line-node  $d$ -wave model (see blue line). In case of an  $s$ - or  $p$ -wave model, we also find a poor agreement with the data below  $T/T_c \approx 0.3$  (see green and yellow lines). For the two-gap scenario, we consider here the so-called  $\alpha$  model. In this case, the superfluid density can be described by  $\rho_{\text{sc}}(T) = w\rho_{\text{sc}}^{\Delta^f}(T) + (1 - w)\rho_{\text{sc}}^{\Delta^s}(T)$ , where  $\rho_{\text{sc}}^{\Delta^f}$  and  $\rho_{\text{sc}}^{\Delta^s}$  are the superfluid densities related to the first ( $\Delta^f$ ) and second ( $\Delta^s$ ) gaps, and  $w$  is a relative weight. For each gap,  $\rho_{\text{sc}}(T)$  is given by Eq. (2). The superfluid density is best fit by a two-gap ( $s + d$ )-wave model (see black line), while the ( $s + s$ )-wave model (see red line) shows a clear deviation from the low- $T$  data [see enlarged plot in the inset of Fig. 6(a)]. This is also reflected in the smallest  $\chi_r^2$  value for the ( $s + d$ )-wave model (see details in Table I). Note that, although in general the ( $s + p$ )-wave model also can describe the data reasonably well, it is inconsistent with the preserved time-reversal symmetry (TRS) in the superconducting state of  $\text{CuIr}_2\text{Te}_4$  (see below). This is different from the case of  $\text{CaPtAs}$  superconductor, where the ( $s + p$ )-wave model was proposed to account for both the gap nodes and broken TRS in the superconducting state [44]. In the TF-80 mT  $\mu\text{SR}$  case [see Fig. 6(b)], the increased magnetic field suppresses the  $s$ -type gap from  $1.75k_B T_c$  to  $1.3k_B T_c$ , while the  $d$ -type gap and its weight remain the same (see weights reported in Table I). The separate  $s$  and  $d$  components of the superfluid density are shown by dotted and dash-dotted lines in Fig. 6(b). The suppression of the  $s$ -type gap at 80 mT makes the nodal features more evident in the superfluid density; nevertheless, further low- $T$  measurements (below 0.3 K) are crucial.

To search for a possible breaking of the time-reversal symmetry (TRS) in the superconducting state of  $\text{CuIr}_2\text{Te}_4$ , ZF- $\mu\text{SR}$  measurements were performed in its normal- and superconducting states. As shown in Fig. 7,

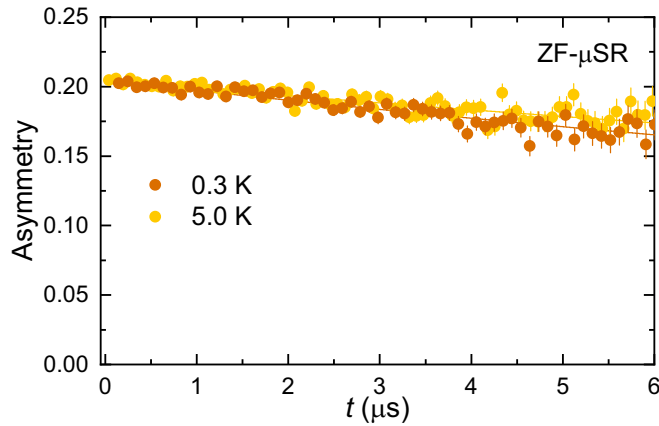


FIG. 7. ZF- $\mu$ SR spectra collected in the superconducting (0.3 K) and the normal (5 K) states of  $\text{CuIr}_2\text{Te}_4$ . The practically overlapping datasets indicate the absence of TRS breaking, whose occurrence would have resulted in a stronger decay in the 0.3-K case.

neither coherent oscillations nor fast decays could be identified in the spectra collected below (0.3 K) and above  $T_c$  (5 K), thus excluding any type of magnetic order or fluctuations. In case of nonmagnetic materials, in the absence of applied fields, the depolarization of muon spins is mainly determined by the randomly oriented nuclear magnetic moments. In  $\text{CuIr}_2\text{Te}_4$ , the depolarization shown in Fig. 7 is more consistent with a Lorentzian decay. This suggests that the internal fields sensed by the implanted muons arise from the diluted (and tiny) nuclear moments present in  $\text{CuIr}_2\text{Te}_4$ . Thus, the solid lines in Fig. 7 are fits to a Lorentzian Kubo-Toyabe relaxation function  $A(t) = A_s[\frac{1}{3} + \frac{2}{3}(1 - \Lambda_{\text{ZF}}t)e^{-\Lambda_{\text{ZF}}t}] + A_{\text{bg}}$ . Here,  $A_s$  and  $A_{\text{bg}}$  are the same as in the TF- $\mu$ SR case [see Eq. (1)], while  $\Lambda_{\text{ZF}}$  represents the ZF Lorentzian relaxation rate. The derived relaxation rates in the normal and the superconducting states are almost identical, i.e.,  $\Lambda_{\text{ZF}} = 0.0263(16) \mu\text{s}^{-1}$  at 0.3 K, and  $\Lambda_{\text{ZF}} = 0.0267(14) \mu\text{s}^{-1}$  at 5 K, as also reflected in the overlapping datasets. The lack of an additional  $\mu$ SR relaxation below  $T_c$  excludes a possible TRS breaking in the superconducting state of  $\text{CuIr}_2\text{Te}_4$ . As a consequence, by taking into account the preserved TRS in  $\text{CuIr}_2\text{Te}_4$ , we have to exclude the  $(s+p)$ -wave model, since only the  $(s+d)$ -wave model is compatible with the experiment.

### C. Electronic specific heat

To further validate the superconducting pairing of  $\text{CuIr}_{2-x}\text{Ru}_x\text{Te}_4$ , its zero-field electronic specific heat  $C_e/T$  was analyzed using the aforementioned models. To subtract the phonon contribution from the specific heat, the normal-state specific heat was fit to the expression  $C/T = \gamma_n + \beta T^2 + \delta T^4$ , with  $\gamma_n$  being the normal-state electronic specific-heat coefficient,  $\beta$  and  $\delta$  the phonon specific-heat coefficients (see dashed lines in the insets of Fig. 8). From this, we derive  $\gamma_n = 13.1(7) \text{ mJ}/(\text{mol K}^2)$ ,  $\beta = 1.63(6) \text{ mJ}/(\text{mol K}^4)$ , and  $\delta = 0.010(1) \text{ mJ}/(\text{mol K}^6)$  for  $\text{CuIr}_2\text{Te}_4$ , while for  $\text{CuIr}_{1.95}\text{Ru}_{0.05}\text{Te}_4$ ,  $\gamma_n = 12.6(1) \text{ mJ}/(\text{mol K}^2)$ ,  $\beta = 1.66(1) \text{ mJ}/(\text{mol K}^4)$ , and  $\delta = 0.011(1) \text{ mJ}/(\text{mol K}^6)$ . After subtracting the phonon contribution ( $\beta T^2 + \delta T^4$ ) from

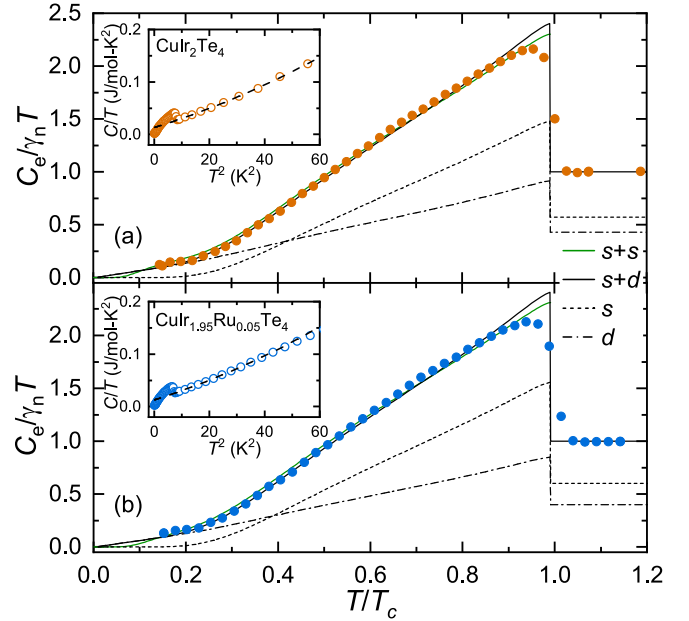


FIG. 8. Normalized electronic specific heat  $C_e/\gamma_n T$  as a function of reduced temperature  $T/T_c$  for (a)  $\text{CuIr}_2\text{Te}_4$  and (b)  $\text{CuIr}_{1.95}\text{Ru}_{0.05}\text{Te}_4$ . The insets show the measured specific heat  $C/T$  versus  $T^2$ . The dashed lines in the insets are fits to  $C/T = \gamma_n + \beta T^2 + \delta T^4$  for  $T > T_c$ . The solid green and black lines represent the electronic specific heat calculated by considering a two-gap  $(s+s)$ - and  $(s+d)$ -wave model, respectively. The dashed- and dash-dotted lines show the individual contributions from the  $s$ - and  $d$ -type SC gaps for the  $(s+d)$ -wave model. The fitting parameters are listed in Table I.

the raw data, the electronic specific heat divided by  $\gamma_n$ , i.e.,  $C_e/\gamma_n T$ , is obtained. This is shown in Fig. 8 vs the reduced temperature  $T/T_c$  for both  $\text{CuIr}_2\text{Te}_4$  and  $\text{CuIr}_{1.95}\text{Ru}_{0.05}\text{Te}_4$ .

The contribution of the superconducting phase to entropy can be calculated following the BCS expression [42]

$$S(T) = -\frac{6\gamma_n}{\pi^2 k_B} \int_0^\infty [f \ln f + (1-f) \ln(1-f)] d\epsilon, \quad (3)$$

where  $f$  is the same as in Eq. (2). Then, the temperature-dependent electronic specific heat in the superconducting state can be calculated from  $C_e = T \frac{dS}{dT}$ . In case of a multiple-gap model, the electronic specific heat can be modeled by  $C_e(T)/T = w C_e^{\Delta^f}(T)/T + (1-w) C_e^{\Delta^s}(T)/T$  [45]. Here, each term represents the contribution to the specific heat of the individual gaps, with  $w$ ,  $\Delta^f$ , and  $\Delta^s$  being the same parameters as for the superfluid-density fits. To analyze the electronic specific heat, we employ the same models used to fit the superfluid density. The fit parameters obtained in both cases are listed in Table I. Also for the specific heat, the single-gap  $s$ -,  $p$ -, and  $d$ -wave models deviate significantly from the data, here reflected in larger  $\chi_r^2$  values. Conversely, the multigap models exhibit a much better agreement with the experimental data across the full temperature range, with the  $(s+d)$ -wave model (solid-black lines) showing the smallest deviation (i.e., smallest  $\chi_r^2$ ). While the  $(s+s)$ -wave model (solid-green lines) reproduces the data for  $T/T_c \gtrsim 0.6$ , it deviates from them at

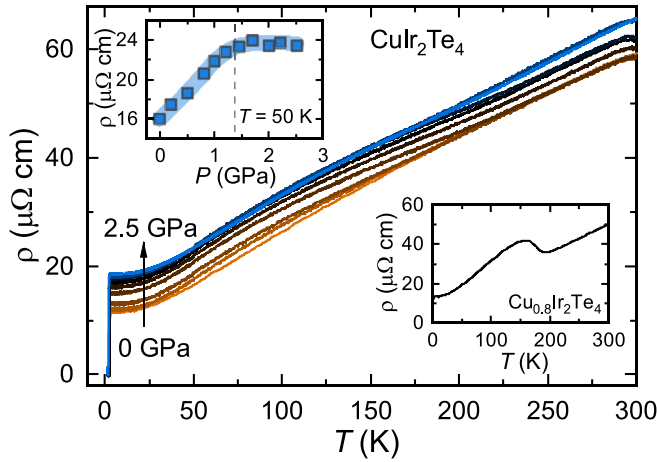


FIG. 9. Temperature-dependent electrical resistivity measured under various external pressures up to 2.5 GPa for  $\text{CuIr}_2\text{Te}_4$ . The upper inset summarizes the 50-K electrical-resistivity vs pressure. The lower inset shows the electrical resistivity for  $\text{Cu}_{0.8}\text{Ir}_2\text{Te}_4$ , where the hump at  $\approx 190$  K indicates the CDW transition.

low temperatures, hence yielding a slightly larger  $\chi_r^2$  than the two-gap ( $s + d$ )-wave model (see Table I). In summary, both the temperature-dependent superfluid density and electronic specific heat are well described by a two-gap ( $s + d$ )-wave model, hence providing strong evidence about nodal superconductivity in  $\text{CuIr}_{1-x}\text{Ru}_x\text{Te}_4$ . Incidentally, the multigap features are also reflected in the temperature-dependent upper critical field of  $\text{CuIr}_{1-x}\text{Ru}_x\text{Te}_4$  (see details in Fig. 4).

#### D. Pressure effects

We also investigated the pressure effects on the normal and superconducting states of  $\text{CuIr}_2\text{Te}_4$ . As shown in Fig. 9, the temperature-dependent electrical resistivity was measured at various external pressures up to 2.5 GPa. At ambient pressure,  $\rho(T)$  shows the typical behavior of metallic compounds, with no peculiar features related to possible phase transitions in the normal state. Previous studies report a dramatic jump in  $\rho(T)$  near 250 K, attributed to the CDW transition [16,19,20]. In our case, the absence of a CDW anomaly might be due to a slightly different Cu content. Indeed, our preliminary electrical-resistivity measurements on  $\text{Cu}_{0.8}\text{Ir}_2\text{Te}_4$  reveal a clear CDW transition at  $\approx 190$  K (see bottom inset in Fig. 9). As the pressure increases to  $\approx 1.2$  GPa,  $\rho(T)$  exhibits a broad hump around 100 K, most likely related to the CDW transition. As the pressure increases further, the hump shifts to higher temperatures. The top inset in Fig. 9 summarizes the dependence of the 50-K electrical resistivity on external pressure. First, the electrical resistivity increases with pressure. Then, above 1.2 GPa, where the resistive hump becomes more evident, it starts to saturate. Such behavior is consistent with previous chemical-pressure studies on  $\text{CuIr}_2\text{Te}_4$ , indicating that both S-Te and Se-Te substitutions favor the CDW order [46,47]. Figure 10 shows the low- $T$  (below 4 K) electrical resistivity and ac susceptibility collected at various applied pressures. As the pressure increases, the superconducting transition, in both  $\rho(T)$  and  $\chi'(T)$ , becomes broader and  $T_c$  is progressively suppressed to lower temperatures. Similar to

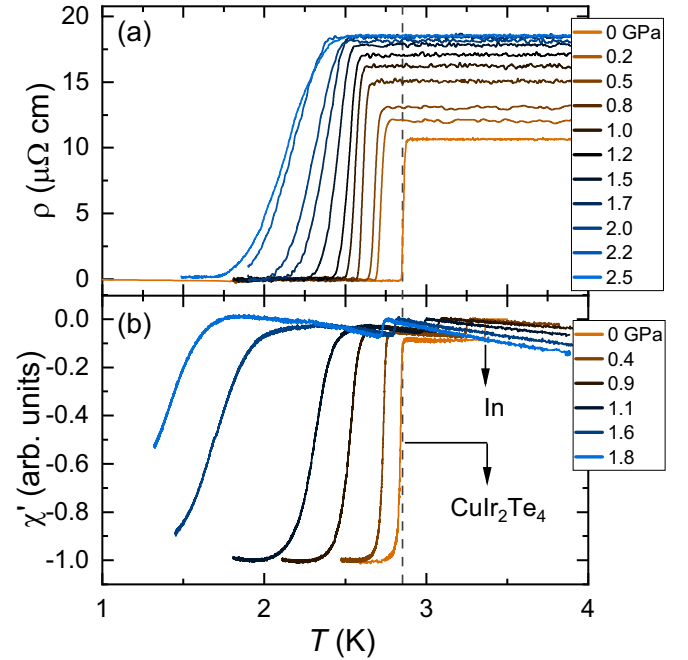


FIG. 10. (a) Low- $T$  electrical resistivity  $\rho(T)$  and (b) real part of ac susceptibility  $\chi'(T)$ , collected under applied pressure up to 2.5 GPa.  $T_c$  was defined as the onset of zero resistivity in the  $\rho(T)$  curves, or as the onset of superconducting transition in the  $\chi'(T)$  curves (both marked by a dashed line for the ambient-pressure case). The SC transition of indium is used to determine the applied pressure during the  $\chi'(T)$  measurements.

the ambient-pressure case (see details in Fig. 3), the  $T_c$  is again defined as the onset of zero resistivity. This coincides with the onset of superconducting transition in  $\chi'(T)$  and is indicated by dashed lines in the two panels of Fig. 10. These highly consistent  $T_c$  values versus the applied pressure are summarized in Fig. 11(a). The  $T_c(P)$  exhibits a decreasing nonlinear trend, starting at 2.85 K at ambient pressure to reach 1.72 K at 2.5 GPa. As shown in Fig. 11(b), we measured also the electrical resistivity at 2.2 GPa under increasingly higher magnetic fields, up to 0.15 T. Interestingly, the  $H_{c2}(T)$  under applied pressure is significantly different from the ambient-pressure case.  $H_{c2}(T)$  at 2.2 GPa is well described by the WHH model [see solid line in Fig. 11(c)], more consistent with a single-band  $s$ -wave superconductor. Conversely, at ambient pressure, the linear dependence of  $H_{c2}(T)$  is attributed to multiple gaps and unconventional pairing. This suggests that pressure most likely suppresses the nodal component of superconductivity, thus changing its character from partially nodal towards fully gapped.

#### E. Discussion

According to the temperature-dependent superfluid density and zero-field electronic specific-heat data,  $\text{CuIr}_2\text{Te}_4$  exhibits a multigap SC, best described by an ( $s + d$ )-wave model. In both cases, the presence of gap nodes and thus, of low-energy excitations, is reflected in a weak (i.e., nonconstant) temperature dependence for  $T < T_c/3$  (see details in Figs. 6 and 8). The multigap nature of SC is further confirmed by the

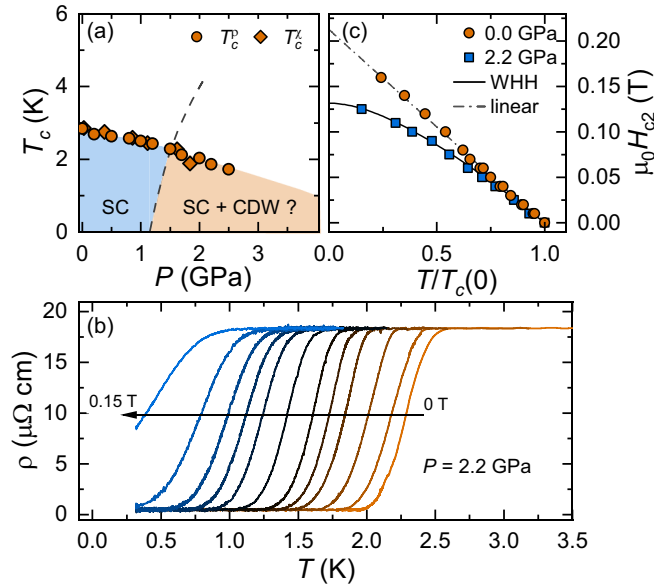


FIG. 11. (a) Superconducting transition temperature  $T_c$  vs external pressure.  $T_c$  was determined from the measurements shown in Fig. 10. (b) Temperature-dependent electrical resistivity at 2.2 GPa measured under various magnetic fields, up to 0.15 T. (c) Upper critical field  $H_{c2}$  vs the reduced transition temperature  $T_c/T_c(0)$  for  $\text{CuIr}_2\text{Te}_4$  at ambient pressure and at 2.2 GPa. The solid line represents a fit to the WHH model, while the dash-dotted line indicates a linear temperature dependence.

temperature-dependent upper critical field (see Fig. 4). In both  $\text{CuIr}_2\text{Te}_4$  and  $\text{CuIr}_{0.95}\text{Ru}_{0.05}\text{Te}_4$ , the two-band model is clearly superior to the WHH model in the low- $T$  and/or high-field region. In the  $\text{CuIr}_2\text{Te}_4$  case, also the electronic band-structure calculations support a multigap SC, since they indicate that multiple bands cross the Fermi level [16]. In our case, a linear  $H_{c2}(T)$  over a wide temperature range departs significantly from the  $H_{c2}(T)$  of most BCS superconductors and is likely attributed to the presence of nodes in the superconducting gap. As recently shown in  $\text{ThCo}_{1-x}\text{Ni}_x\text{C}_2$  superconductors, a linear  $H_{c2}(T)$  was proposed to be closely related to a  $d$ -wave pairing [29,30]. Which electronic bands account for the  $s$ -wave and  $d$ -wave pairing in  $\text{CuIr}_2\text{Te}_4$  is not yet known and requires further theoretical investigation.

$H_{c2}(T)$  measured under applied pressure differs significantly from that measured at ambient pressure. For instance, at 2.2 GPa,  $H_{c2}(T)$  follows very well the WHH model [see details in Fig. 11(c)], more consistent with a single-band  $s$ -wave superconductor. As proposed in Fig. 11(a), in the low-pressure region,  $\text{CuIr}_2\text{Te}_4$  shows a pure superconducting phase below  $T_c$ . As the pressure increases towards 1.2 GPa, a CDW order starts to develop and, at higher applied pressures, the SC phase might coexist with the CDW phase, hence, becoming more conventional. The dashed line in Fig. 11(a) separates these qualitatively different SC phases. Eventually, at even higher pressures (around 4.5 GPa) the CDW phase becomes dominant and entirely suppresses the SC phase (to be confirmed experimentally). A similar phase diagram is shown by the isostructural  $\text{Ir}_{0.95}\text{Pt}_{0.05}\text{Te}_2$  compounds, where again the external pressure suppresses the superconductivity

and gives rise to a CDW order [48]. In the low-pressure region, the unconventional ( $s + d$ )-wave pairing of  $\text{CuIr}_2\text{Te}_4$  might reflect the ubiquitous charge fluctuations near the CDW quantum critical point. A further increase in pressure quenches these fluctuations and makes the  $s$ -wave pairing more favorable. By contrast, in the  $(\text{Ca}_{1-x}\text{Sr}_x)_3\text{Ir}_4\text{Sn}_{13}$  family, despite a similar phase diagram to  $\text{CuIr}_2\text{Te}_4$  [49], the superconducting order parameter of both the pure-SC and of the SC + CDW phase maintains the same  $s$ -wave character [50]. Consequently,  $\text{CuIr}_2\text{Te}_4$  might represent a rare case, where the SC and SC + CDW phases show different superconducting pairings. To prove such a scenario, it would be interesting to investigate the evolution of the superconducting pairing in  $\text{CuIr}_2\text{Te}_4$  under applied pressure, e.g., via TF- $\mu$ SR measurements under pressure. Alternatively, TF- $\mu$ SR measurements on  $\text{CuIr}_2\text{Te}_{4-x}(\text{Se}, \text{S})_x$ , where multiple CDW phases are known to coexist with SC [46,47], would also provide important hints on the superconducting pairing.

#### IV. CONCLUSION

In summary, we investigated the normal and the superconducting properties of  $\text{CuIr}_{2-x}\text{Ru}_x\text{Te}_4$  ( $x = 0, 0.05$ ) by means of electrical resistivity, magnetization, heat-capacity, and  $\mu$ SR measurements.  $\text{CuIr}_2\text{Te}_4$  and  $\text{CuIr}_{1.95}\text{Ru}_{0.05}\text{Te}_4$  exhibit bulk superconductivity with  $T_c = 2.85$  and 2.7 K, respectively. Both the temperature-dependent superfluid density and the electronic specific heat are best described by a two-gap model [here, ( $s + d$ ) wave], comprising a nodeless gap and a gap with nodes, rather than by single-band models. The multigap SC in  $\text{CuIr}_{2-x}\text{Ru}_x\text{Te}_4$  is further supported by the temperature dependence of the upper critical field  $H_{c2}(T)$ . The application of external pressure promotes the formation of CDW order and shifts  $\text{CuIr}_2\text{Te}_4$  towards a conventional  $s$ -wave SC behavior. The unconventional superconducting pairing in  $\text{CuIr}_{2-x}\text{Ru}_x\text{Te}_4$  seems closely related to the charge fluctuations occurring near the CDW quantum critical point. Finally, the absence of spontaneous magnetic fields below the onset of superconductivity, as inferred from zero-field  $\mu$ SR measurements, confirms that time-reversal symmetry is preserved in the superconducting state of  $\text{CuIr}_{2-x}\text{Ru}_x\text{Te}_4$ .

#### ACKNOWLEDGMENTS

This work was supported by the Natural Science Foundation of Shanghai (Grants No. 21ZR1420500 and No. 21JC1402300), the Fundamental Research Funds for the Central Universities, and the Schweizerische Nationalfonds zur Förderung der Wissenschaftlichen Forschung (SNF) (Grants No. 200021\_188706 and No. 206021\_139082). H.Q.Y. acknowledges support from the National Key R&D Program of China (Grants No. 2017YFA0303100 and No. 2016YFA0300202), the Key R&D Program of Zhejiang Province, China (Grant No. 2021C01002), the National Natural Science Foundation of China (Grant No. 11974306). Y.X. acknowledges support from the National Natural Science Foundation of China (Grant No. 12274125) and the Shanghai Pujiang Program (Grant No. 21PJ1403100).



- [1] P. Monthoux, D. Pines, and G. G. Lonzarich, Superconductivity without phonons, *Nature (London)* **450**, 1177 (2007).
- [2] I. I. Mazin, Superconductivity gets an iron boost, *Nature (London)* **464**, 183 (2010).
- [3] B. Keimer, S. A. Kivelson, M. R. Norman, S. Uchida, and J. Zaanen, From quantum matter to high-temperature superconductivity in copper oxides, *Nature (London)* **518**, 179 (2015).
- [4] R. M. Fernandes, A. V. Chubukov, and J. Schmalian, What drives nematic order in iron-based superconductors?, *Nat. Phys.* **10**, 97 (2014).
- [5] E. Morosan, H. W. Zandbergen, B. S. Dennis, J. W. G. Bos, Y. Onose, T. Klimczuk, A. P. Ramirez, N. P. Ong, and R. J. Cava, Superconductivity in  $\text{Cu}_x\text{TiSe}_2$ , *Nat. Phys.* **2**, 544 (2006).
- [6] K. Cho, M. Kończykowski, S. Teknowijoyo, M. A. Tanatar, J. Guss, P. B. Gartin, J. M. Wilde, A. Kreyssig, R. J. McQueeney, A. I. Goldman, V. Mishra, P. J. Hirschfeld, and R. Prozorov, Using controlled disorder to probe the interplay between charge order and superconductivity in  $\text{NbSe}_2$ , *Nat. Commun.* **9**, 2796 (2018).
- [7] B. R. Ortiz, S. M. L. Teicher, Y. Hu, J. L. Zuo, P. M. Sarte, E. C. Schueller, A. M. M. Abeykoon, M. J. Krogstad, S. Rosenkranz, R. Osborn, R. Seshadri, L. Balents, J. He, and S. D. Wilson,  $\text{CsV}_3\text{Sb}_5$ : A  $\mathbb{Z}_2$  Topological Kagome Metal with a Superconducting Ground State, *Phys. Rev. Lett.* **125**, 247002 (2020).
- [8] Y.-X. Jiang, J.-X. Yin, M. M. Denner, N. Shumiya, B. R. Ortiz, G. Xu, Z. Guguchia, J. He, M. S. Hossain, X. Liu, J. Ruff, L. Kautzsch, S. S. Zhang, G. Chang, I. Belopolski, Q. Zhang, T. A. Cochran, D. Multer, M. Litskevich, Z.-J. Cheng, *et al.*, Unconventional chiral charge order in kagome superconductor  $\text{KV}_3\text{Sb}_5$ , *Nat. Mater.* **20**, 1353 (2021).
- [9] L. Nie, K. Sun, W. Ma, D. Song, L. Zheng, Z. Liang, P. Wu, F. Yu, J. Li, M. Shan, D. Zhao, S. Li, B. Kang, Z. Wu, Y. Zhou, K. Liu, Z. Xiang, J. Ying, Z. Wang, T. Wu *et al.*, Charge-density-wave-driven electronic nematicity in a kagome superconductor, *Nature (London)* **604**, 59 (2022).
- [10] S. Nagata, T. Hagino, Y. Seki, and T. Bitoh, Metal-insulator transition in thiospinel  $\text{CuIr}_2\text{S}_4$ , *Phys. B (Amsterdam, Neth.)* **194-196**, 1077 (1994).
- [11] T. Furubayashi, T. Matsumoto, T. Hagino, and S. Nagata, Structural and magnetic studies of metal-insulator transition in thiospinel  $\text{CuIr}_2\text{S}_4$ , *J. Phys. Soc. Jpn.* **63**, 3333 (1994).
- [12] S. Nagata, N. Matsumoto, Y. Kato, T. Furubayashi, T. Matsumoto, J. P. Sanchez, and P. Vulliet, Metal-insulator transition in the spinel-type  $\text{CuIr}_2(\text{S}_{1-x}\text{Se}_x)_4$  system, *Phys. Rev. B* **58**, 6844 (1998).
- [13] H. Suzuki, T. Furubayashi, G. Cao, H. Kitazawa, A. Kamimura, K. Hirata, and T. Matsumoto, Metal-insulator transition and superconductivity in spinel-type system  $\text{Cu}_{1-x}\text{Zn}_x\text{Ir}_2\text{S}_4$ , *J. Phys. Soc. Jpn.* **68**, 2495 (1999).
- [14] H. Luo, T. Klimczuk, L. Muehler, L. Schoop, D. Hirai, M. K. Fuccillo, C. Felser, and R. J. Cava, Superconductivity in the  $\text{Cu}(\text{Ir}_{1-x}\text{Pt}_x)_2\text{Se}_4$  spinel, *Phys. Rev. B* **87**, 214510 (2013).
- [15] R. M. Fleming, F. J. DiSalvo, R. J. Cava, and J. V. Waszczak, Observation of charge-density waves in the cubic spinel structure  $\text{CuV}_2\text{S}_4$ , *Phys. Rev. B* **24**, 2850 (1981).
- [16] D. Yan, Y. Zeng, G. Wang, Y. Liu, J. Yin, T.-R. Chang, H. Lin, M. Wang, J. Ma, S. Jia, D.-X. Yao, and H. Luo,  $\text{CuIr}_2\text{Te}_4$ : A quasi-two-dimensional ternary telluride chalcogenide superconductor, [arXiv:1908.05438](https://arxiv.org/abs/1908.05438).
- [17] Y. S. Hor, A. J. Williams, J. G. Checkelsky, P. Roushan, J. Seo, Q. Xu, H. W. Zandbergen, A. Yazdani, N. P. Ong, and R. J. Cava, Superconductivity in  $\text{Cu}_x\text{Bi}_2\text{Se}_3$  and its Implications for Pairing in the Undoped Topological Insulator, *Phys. Rev. Lett.* **104**, 057001 (2010).
- [18] S. Sasaki, M. Kriener, K. Segawa, K. Yada, Y. Tanaka, M. Sato, and Y. Ando, Topological Superconductivity in  $\text{Cu}_x\text{Bi}_2\text{Se}_3$ , *Phys. Rev. Lett.* **107**, 217001 (2011).
- [19] S. Nagata, N. Kijima, S. Ikeda, N. Matsumoto, R. Endoh, S. Chikazawa, I. Shimono, and H. Nishihara, Resistance anomaly in  $\text{CuIr}_2\text{Te}_4$ , *J. Phys. Chem. Solids* **60**, 163 (1999).
- [20] D. Yan, L. Zeng, Y. Lin, J. Yin, Y. He, X. Zhang, M. Huang, B. Shen, M. Wang, Y. Wang, D. Yao, and H. Luo, Superconductivity in Ru-doped  $\text{CuIr}_2\text{Te}_4$  telluride chalcogenide, *Phys. Rev. B* **100**, 174504 (2019).
- [21] L. Zeng, D. Yan, Y. He, M. Boubeche, Y. Huang, X. Wang, and H. Luo, Effect of Ti substitution on the superconductivity of  $\text{CuIr}_2\text{Te}_4$  telluride chalcogenide, *J. Alloys Compd.* **885**, 160981 (2021).
- [22] D. Yan, L. Zeng, Y. Zeng, Y. Lin, J. Yin, M. Wang, Y. Wang, D. Yao, and H. Luo, Superconductivity in  $\text{CuIr}_{2-x}\text{Al}_x\text{Te}_4$  telluride chalcogenides, *Chin. Phys. B* **31**, 037406 (2022).
- [23] L. Zeng, Y. Ji, D. Yu, S. Guo, Y. He, K. Li, Y. Huang, C. Zhang, P. Yu, S. Luo, H. Wang, and H. Luo, Negative chemical pressure effect on the superconductivity and charge density wave of  $\text{Cu}_{0.5}\text{Ir}_{1-x}\text{Zr}_x\text{Te}_2$ , *J. Phys. Chem. C* **126**, 3705 (2022).
- [24] L. Zeng, X. Hu, N. Wang, J. Sun, P. Yang, M. Boubeche, S. Luo, Y. He, J. Cheng, D.-X. Yao, and H. Luo, Interplay between charge-density-wave, superconductivity, and ferromagnetism in  $\text{CuIr}_{2-x}\text{Cr}_x\text{Te}_4$  chalcogenides, *J. Phys. Chem. Lett.* **13**, 2442 (2022).
- [25] A. Suter and B. M. Wojek, Musrfit: A free platform-independent framework for  $\mu$  SR data analysis, *Phys. Procedia* **30**, 69 (2012).
- [26] N. R. Werthamer, E. Helfand, and P. C. Hohenberg, Temperature and purity dependence of the superconducting critical field,  $H_{c2}$ . III. Electron spin and spin-orbit effects, *Phys. Rev.* **147**, 295 (1966).
- [27] W. Sun, Y. Li, R. Liu, J. Yang, J. Li, S. Yan, H. Sun, W. Guo, Z. Gu, Y. Deng, X. Wang, and Y. Nie, Evidence for quasi-two-dimensional superconductivity in infinite-layer nickelates, [arXiv:2204.13264](https://arxiv.org/abs/2204.13264).
- [28] L. E. Chow, K. Y. Yip, M. Pierre, S. W. Zeng, Z. T. Zhang, T. Heil, J. Deuschle, P. Nandi, S. K. Sudheesh, Z. S. Lim, Z. Y. Luo, M. Nardone, A. Zitouni, P. A. van Aken, M. Goiran, S. K. Goh, W. Escoffier, and A. Ariando, Pauli-limit violation in lanthanide infinite-layer nickelate superconductors, [arXiv:2204.12606](https://arxiv.org/abs/2204.12606).
- [29] T. W. Grant, O. V. Cigarroa, P. F. S. Rosa, A. J. S. Machado, and Z. Fisk, Tuning of superconductivity by Ni substitution into noncentrosymmetric  $\text{ThCo}_{1-x}\text{Ni}_x\text{C}_2$ , *Phys. Rev. B* **96**, 014507 (2017).
- [30] A. Bhattacharyya, D. T. Adroja, K. Panda, S. Saha, T. Das, A. J. S. Machado, O. V. Cigarroa, T. W. Grant, Z. Fisk, A. D. Hillier, and P. Manfrinetti, Evidence of a Nodal Line in the Superconducting Gap Symmetry of Noncentrosymmetric  $\text{ThCoC}_2$ , *Phys. Rev. Lett.* **122**, 147001 (2019).
- [31] K.-H. Müller, G. Fuchs, A. Handstein, K. Nenkov, V. N. Narozhnyi, and D. Eckert, The upper critical field in superconducting  $\text{MgB}_2$ , *J. Alloys Compd.* **322**, L10 (2001).

- [32] Y. Nakajima, H. Hidaka, T. Nakagawa, T. Tamegai, T. Nishizaki, T. Sasaki, and N. Kobayashi, Two-band superconductivity featuring different anisotropies in the ternary iron silicide  $\text{Lu}_2\text{Fe}_3\text{Si}_5$ , *Phys. Rev. B* **85**, 174524 (2012).
- [33] A. Gurevich, Iron-based superconductors at high magnetic fields, *Rep. Prog. Phys.* **74**, 124501 (2011), and references therein.
- [34] A. Yaouanc and P. D. de Réotier, *Muon Spin Rotation, Relaxation, and Resonance: Applications to Condensed Matter* (Oxford University Press, Oxford, 2011).
- [35] A. Amato, Heavy-fermion systems studied by  $\mu$  SR technique, *Rev. Mod. Phys.* **69**, 1119 (1997).
- [36] S. J. Blundell, Spin-polarized muons in condensed matter physics, *Contemp. Phys.* **40**, 175 (1999).
- [37] A. Maisuradze, R. Khasanov, A. Shengelaya, and H. Keller, Comparison of different methods for analyzing  $\mu$  SR line shapes in the vortex state of type-II superconductors, *J. Phys.: Condens. Matter* **21**, 075701 (2009).
- [38] T. Shang, J. Philippe, J. A. T. Verezhak, Z. Guguchia, J. Z. Zhao, L.-J. Chang, M. K. Lee, D. J. Gawryluk, E. Pomjakushina, M. Shi, M. Medarde, H.-R. Ott, and T. Shiroka, Nodeless superconductivity and preserved time-reversal symmetry in the noncentrosymmetric  $\text{Mo}_3\text{P}$  superconductor, *Phys. Rev. B* **99**, 184513 (2019).
- [39] T. Shang, A. Amon, D. Kasinathan, W. Xie, M. Bobnar, Y. Chen, A. Wang, M. Shi, M. Medarde, H. Q. Yuan, and T. Shiroka, Enhanced  $T_c$  and multiband superconductivity in the fully-gapped  $\text{ReBe}_{22}$  superconductor, *New J. Phys.* **21**, 073034 (2019).
- [40] W. Barford and J. M. F. Gunn, The theory of the measurement of the London penetration depth in uniaxial type-II superconductors by muon spin rotation, *Phys. C (Amsterdam, Neth.)* **156**, 515 (1988).
- [41] E. H. Brandt, Properties of the ideal Ginzburg-Landau vortex lattice, *Phys. Rev. B* **68**, 054506 (2003).
- [42] M. Tinkham, *Introduction to Superconductivity*, 2nd ed. (Dover Publications, Mineola, 1996).
- [43] A. Carrington and F. Manzano, Magnetic penetration depth of  $\text{MgB}_2$ , *Phys. C (Amsterdam, Neth.)* **385**, 205 (2003).
- [44] T. Shang, M. Smidman, A. Wang, L.-J. Chang, C. Baines, M. K. Lee, Z. Y. Nie, G. M. Pang, W. Xie, W. B. Jiang, M. Shi, M. Medarde, T. Shiroka, and H. Q. Yuan, Simultaneous Nodal Superconductivity and Time-Reversal Symmetry Breaking in the Noncentrosymmetric Superconductor  $\text{CaPtAs}$ , *Phys. Rev. Lett.* **124**, 207001 (2020).
- [45] F. Bouquet, Y. Wang, R. A. Fisher, D. G. Hinks, J. D. Jorgensen, A. Junod, and N. E. Phillips, Phenomenological two-gap model for the specific heat of  $\text{MgB}_2$ , *Europhys. Lett.* **56**, 856 (2001).
- [46] M. Boubeche, N. Wang, J. Sun, P. Yang, L. Zeng, Q. Li, Y. He, S. Luo, J. Cheng, Y. Peng, and H. Luo, Anomalous charge density wave state evolution and dome-like superconductivity in  $\text{CuIr}_2\text{Te}_{4-x}\text{Se}_x$  chalcogenides, *Supercond. Sci. Technol.* **34**, 115003 (2021).
- [47] M. Boubeche, N. Wang, J. Sun, P. Yang, L. Zeng, S. Luo, Y. He, J. Yu, M. Wang, J. Cheng, and H. Luo, Superconducting dome associated with the suppression and re-emergence of charge density wave states upon sulfur substitution in  $\text{CuIr}_2\text{Te}_{4-x}\text{S}_x$  chalcogenides, *J. Phys.: Condens. Matter* **34**, 205602 (2022).
- [48] O. Ivashko, L. Yang, D. Destraz, E. Martino, Y. Chen, C. Y. Guo, H. Q. Yuan, A. Pisoni, P. Matus, S. Pyon, K. Kudo, M. Nohara, L. Forró, H. M. Rønnow, M. Hücker, M. v. Zimmermann, and J. Chang, Charge-stripe order and superconductivity in  $\text{Ir}_{1-x}\text{Pt}_x\text{Te}_2$ , *Sci. Rep.* **7**, 17157 (2017).
- [49] L. E. Klintberg, S. K. Goh, P. L. Alireza, P. J. Saines, D. A. Tompsett, P. W. Logg, J. Yang, B. Chen, K. Yoshimura, and F. M. Grosche, Pressure- and Composition-Induced Structural Quantum Phase Transition in the Cubic Superconductor  $(\text{Ca,Sr})_3\text{Ir}_4\text{Sn}_{13}$ , *Phys. Rev. Lett.* **109**, 237008 (2012).
- [50] P. K. Biswas, Z. Guguchia, R. Khasanov, M. Chinotti, L. Li, K. Wang, C. Petrovic, and E. Morenzoni, Strong enhancement of  $s$ -wave superconductivity near a quantum critical point of  $\text{Ca}_3\text{Ir}_4\text{Sn}_{13}$ , *Phys. Rev. B* **92**, 195122 (2015).